Research Square

Preprints are preliminary reports that have not undergone peer review.
They should not be considered conclusive, used to inform clinical practice,
or referenced by the media as validated information.

Room Temperature Corrosion of Iron Foam for Sulfur Anion Modulation of Hydroxysulfide Electrocatalysts for Oxygen Evolution

Pingping Gao
Hunan Institute of Engineering
Quan Kong
Yunnan University
Ting Lei
Central South University
Meilian Gao
Hunan Institute of Engineering
Shuti Ouyang
Central South University
Qinghua Chen
qinghua.chen@zhidebattery.com

Lanxi Zhide New Energy Materials Co., Ltd.

Research Article

Keywords: Water electrolysis, Oxygen evolution reaction, Hydroxysulfide, Sulfur anion modulation

Posted Date: November 20th, 2026

DOI: https://doi.org/10.21203/rs.3.rs-11670738/v1

License: This work is licensed under a Creative Commons Attribution 4.0 International License.
Read Full License

Additional Declarations: No competing interests reported.

Abstract

Ni–Fe-based compounds are promising electrocatalysts for the oxygen evolution reaction (OER) in water electrolysis because of their low cost and tunable intrinsic activity. Here, we use a room-temperature immersion corrosion strategy in which iron foam (FF) serves as both the conductive substrate and the iron source. The slow release of sulfur from thioacetamide enables the insitu growth of sulfur-doped nickel–iron hydroxide (S-NiFe(OH)x) on FF. The optimized S-NiFe(OH)x-0.01/FF electrode requires an overpotential of 236 mV to deliver a current density of 50 mA cm^{-2} in 1 M KOH and exhibits a Tafel slope of 86 mV dec^{-1}. It also shows an overpotential increase of less than 10 mV during 12 h of operation at 50 mA cm^{-2}. Sulfur incorporation modifies the electronic environment of the NiFe sites and is proposed to balance OH^- adsorption and O_2 desorption. This approach combines simple fabrication, inexpensive raw materials, and mild synthesis conditions to prepare efficient transition-metal-based OER electrocatalysts.

1. Introduction

The growing demand for sustainable energy has stimulated research into clean and renewable energy systems[1]. Hydrogen is a promising energy carrier for addressing energy shortages and environmental pollution[2, 3]. Water electrolysis offers a pathway to hydrogen production, but its efficiency is limited by the multielectron anodic oxygen evolution reaction (OER) [4]. Sluggish OER kinetics require a substantial overpotential, reducing overall energy conversion efficiency and potentially compromising electrode durability [5]. Effective electrocatalysts can accelerate the anodic reaction [6]. Transition-metal compounds are promising candidates because of their elemental abundance, accessible synthesis, and catalytic activity [7].

In transition-metal compounds, metal cations generally serve as active sites for the adsorption of hydroxyl intermediates during the OER [8]. Their electronic configuration therefore plays a key role in electrocatalytic performance [9]. Coordinating anions influence the local environment and electronic structure of these cationic sites, making anion engineering an effective strategy for improving catalytic activity [10]. Substituting lattice anions with foreign anions can produce mixed-anion coordination environments with different bonding and polarization characteristics. These environments modify charge distribution at the metal centers and the adsorption energies of reaction intermediates, thereby influencing reaction kinetics [11]. For example, Mu et al. [12] synthesized Fe–S-co-doped NiFe layered double hydroxides through liquid-phase sulfurization. They attributed the disruption of adsorption-energy scaling relationships for OER intermediates to the combined effects of sulfur-anion polarization and Fe active sites. Lattice oxygen also participated in the catalytic cycle, and the coupled adsorbate evolution mechanism (AEM) and lattice oxygen-mediated mechanism (LOM) improved activity and durability at high current densities. Zhang et al. [13] fabricated a self-supported sulfided NiFe coating via high-velocity oxygen fuel spraying combined with gas-phase sulfuration. The coating exhibits outstanding oxygen evolution reaction performance with low overpotential, small Tafel slope, low charge transfer resistance and favorable stability, which originates from the synergistic effect of sulfides and efficient

cleavage of O–O bonds. Zhao et al. [14] developed atomically sulfur-substituted NiFe hydroxysulfide through electrochemical-assisted anion regulation for highly efficient catalysis toward both oxygen evolution and polysulfide redox; nevertheless, such a post-modification strategy suffers from poor scalability and lacks systematic investigations on the phase evolution from atomic doping to sulfide aggregation. However, reported approaches, including hydrothermal sulfurization, high-temperature calcination, and electrochemical treatment, can involve poorly controlled incorporation, structural degradation of layered precursors, or harsh synthesis conditions [15]. These limitations complicate the preparation of uniformly distributed mixed-anion structures. In addition, contact resistance between the catalyst and current collector affects electrode efficiency. Growing the catalyst directly on conductive iron foam can reduce interfacial contact resistance, improve catalyst dispersion and utilization, and enhance electrode stability [16].

Here, we use a mild room-temperature immersion corrosion strategy to grow NiFe(OH)x nanosheet arrays directly on iron foam for the OER. Sulfur incorporation is controlled by varying the precursor concentration to tune the local electronic environment of the active sites. This design draws on the different polarizabilities of oxygen- and sulfur-containing anions: oxygen-containing anions are relatively hard and weakly polarizable, whereas sulfur-containing anions are softer and more polarizable [14, 17]. We propose that partial substitution of oxygen-containing ligands with sulfur-containing species can balance reactant adsorption and product desorption by modifying the electronic structure of the metal sites. Controlling the sulfur precursor concentration also provides a means of limiting sulfide particle formation at higher sulfur loadings.

2. Experimental

2.1 Materials fabrication

All reagents were of analytical grade and used without further purification. Iron foam (FF; thickness, 1 mm; purity, 99.99%) was purchased from Changsha Lyrun Material Co., Ltd. and used as the conductive current collector. Ultrapure water was produced in the laboratory and used for material synthesis.

Iron foam substrates (1 cm × 4 cm) were cleaned sequentially with 2 M hydrochloric acid and absolute ethanol to remove surface contaminants. The substrates were then immersed vertically in 100 mL of an aqueous solution containing 0.05 M $NiCl_2 \cdot 6H_2O$ and 0.01 M thioacetamide (CH_3CSNH_2) and left undisturbed at 25°C for 12 h. The resulting electrode was rinsed repeatedly with deionized water and absolute ethanol and dried at 60°C for 12 h. The sample was designated S-NiFe(OH)x-0.01.

Control samples were prepared under identical conditions, except that the thioacetamide concentration was adjusted to 0, 0.005, 0.025, 0.05, 0.1, 0.2, or 0.4 M. The resulting samples were designated S-NiFe(OH)x-0, S-NiFe(OH)x-0.005, S-NiFe(OH)x-0.025, NiFeS(OH)x-0.05, NiFeS(OH)x-0.1, NiFeS(OH)x-0.2, and NiFeS(OH)x-0.4, respectively. Increasing the sulfur precursor concentration increased sulfur incorporation and eventually led to the formation of crystalline sulfide nanoparticles. Bare iron foam and

commercial RuO_2 were used as reference materials. Figure 1 depicts the fabrication schematic of the materials.

2.2 Materials Characterizations

The crystalline phases were examined by X-ray diffraction (XRD; Rigaku TTRIII) using Cu Kα radiation (λ = 1.540 Å). Sample morphology was characterized by field-emission scanning electron microscopy (FESEM; FEI Nova Nano SEM 450) and transmission electron microscopy (TEM; JEM-2100). Elemental composition and spatial distribution were analyzed by energy-dispersive X-ray spectroscopy (EDS) coupled with TEM. X-ray photoelectron spectroscopy (XPS; ESCALAB 250) was performed at room temperature using an Al Kα source. Binding energies were calibrated against the C 1s peak at 284.6 eV.

Electrochemical measurements were performed using a Parstat 3000A-DX workstation (Princeton Applied Research, USA) in a three-electrode configuration. The as-prepared electrode, a Hg/HgO electrode, and a graphite rod served as the working, reference, and counter electrodes, respectively. Potentials were converted to the reversible hydrogen electrode (RHE) scale using $E_{(RHE)} = E_{(Hg/HgO)} + 0.098V + (0.059V)\times pH$. The OER overpotential was calculated as $\eta_{(OER)} = E(RHE)-1.23V$. All measurements were conducted in O_2-saturated 1.0 M KOH at room temperature. Linear sweep voltammetry (LSV) was performed at 1 mV s^{-1} to evaluate the hydrogen evolution reaction (HER) and OER overpotentials. Cyclic voltammetry (CV) was used for repeated potential cycling. Long-term operational stability was evaluated by galvanostatic chronopotentiometry (CP), which recorded the electrode potential over time. Electrochemical impedance spectroscopy (EIS) data were analyzed using an equivalent circuit to estimate electrolyte resistance, charge-transfer resistance, and other interfacial parameters.

3 Results and Discussion

3.1 Microstructure Characterization

Figure 2 shows the XRD patterns of eight samples prepared with different thioacetamide concentrations. At concentrations of 0, 0.005, 0.01, and 0.025 M, the observed diffraction peaks are consistent with NiFe layered double hydroxide (NiFe-LDH; PDF #51–0463) and FeO(OH) (PDF #34-1266). No characteristic sulfide peaks are detected, indicating that hydroxide phases dominate within this concentration range and that any sulfide present is below the XRD detection limit. At 0.2 and 0.4 M, peaks assigned to $FeNi_2S_4$ (PDF #01-089-2052) and Ni_3S_2 (PDF #01-076-1870) emerge. These crystalline sulfide phases have been reported in heteroanion engineering [18]. Their appearance, together with the disappearance of the hydroxide diffraction signals, indicates a transition toward sulfide-dominated products at high precursor concentrations. Samples prepared with 0.05 and 0.1 M thioacetamide exhibit both hydroxide and sulfide peaks, suggesting that increasing the sulfur precursor concentration promotes crystalline sulfide formation.

SEM was used to examine the morphology of the catalysts. Figures 3a and 3b show S-NiFe(OH)x-0.01/FF at different magnifications. The catalyst uniformly covers the iron foam framework, consistent with direct growth through substrate corrosion. This morphology provides close contact between the catalyst and the conductive substrate and may improve access to active sites. By comparison, NiFeS(OH)x-0.4 exhibits a less uniform coating and localized particle agglomeration (Figs. 3c and 3d).

Figure.4a-4i show SEM and TEM images of samples prepared with low thioacetamide concentrations (0, 0.01, and 0.025 M). The sulfur-free S-NiFe(OH)x-0 sample consists of interlaced nanosheets (Figure. 4a and Figure.4b), with hydroxide phases identified by XRD. Its high-resolution TEM (HRTEM) image shows lattice fringes assigned to the (012) plane of NiFe-LDH (Figure.4c). The sample prepared with 0.01 M thioacetamide retains the nanosheet morphology (Figure.4d and Figure.4e). Its HRTEM image shows NiFe-LDH (012) fringes without identifiable sulfide fringes (Figure.4f). The observed lattice distortion is consistent with sulfur incorporation, although it does not by itself establish substitution at oxygen sites. At 0.025 M, the nanosheet morphology remains intact (Figure.4g and Figure.4h), but additional local lattice fringes assigned to the (113) plane of Ni_3S_2 appear alongside the NiFe-LDH (012) fringes (Figure.4i), suggesting the onset of sulfide formation. The sulfur elemental maps for samples prepared at 0.005–0.05 M (Figure.4j-4m) further illustrate the change from a relatively uniform distribution to localized enrichment as the precursor concentration increases. Among these samples, the 0.01 M sample exhibits the most uniform sulfur distribution.

Figure.5 shows SEM and TEM images of samples prepared with higher thioacetamide concentrations (0.1, 0.2, and 0.4 M). For NiFeS(OH)x-0.1, sulfide nanoparticles are distributed on the NiFe(OH)x nanosheets (Figure.5a and Figure.5b), and HRTEM reveals lattice fringes assigned to nickel sulfide (Figure.5c). At 0.2 M, the particles grow and aggregate into approximately spherical clusters, within which nickel sulfide lattice fringes can be identified (Figure.5d-5f). Further particle growth is observed at 0.4 M (Figure.5g-5i). Together, the results in Figure. 4 and Figure.5 indicate a progression from sulfur-containing hydroxide nanosheets to hydroxide–sulfide composites and increasingly sulfide-rich products as the precursor concentration increases. Thus, varying the thioacetamide concentration provides a simple way to control sulfur incorporation and sulfide formation.

TEM-EDS elemental maps of S-NiFe(OH)x-0.01 show the presence of Fe, Ni, S, and O, consistent with the expected elemental composition (Figure.6). All four elements are distributed relatively uniformly across the nanosheet. The sulfur map shows no obvious localized enrichment at the spatial resolution of the measurement, supporting a uniform sulfur distribution but not, on its own, establishing atomic-scale substitution.

High-resolution XPS was used to examine changes in the electronic environment of samples prepared with low sulfur precursor concentrations (0-0.025 M; Figure.7). The S 2p spectra were fitted with components assigned to metal–sulfur interactions and S–O bonds (Figure.7a). Increasing sulfur incorporation is associated with a shift in the sulfur-related signals toward higher binding energies, whereas the oxygen spectrum shifts toward lower binding energies (Figure.7b). These trends are

consistent with a redistribution of electron density within the mixed-anion environment [19]. In the proposed interpretation, the greater polarizability of sulfur-containing anions alters electron donation to the metal centers and modifies the electronic environment of neighboring oxygen species. Oxygen-containing anions are relatively hard and weakly polarizable, whereas sulfur-containing anions are softer and more polarizable. Introducing sulfur-containing species can therefore change metal–anion interactions and the electronic structure of the metal sites. The Fe 2p and Ni 2p spectra also shift toward lower binding energies (Figure.7c and Figure.7d). Together with the structural characterization, these results support changes in the local chemical environment following sulfur incorporation. However, the binding-energy shifts alone do not establish a unique charge-transfer pathway or atomic substitution mechanism.

3.2. Electrochemical characterizations

The OER performance of the S-NiFe(OH)x/FF electrodes was evaluated in 1 M KOH (Figure.8). Figure.8a compares the LSV curves, corrected using 95% iR compensation, for S-NiFe(OH)x/FF, NiFeS(OH)x/FF, and the RuO_2/FF reference electrode. Samples prepared with low sulfur precursor concentrations exhibit higher activity, with S-NiFe(OH)x-0.01/FF giving the best performance among the tested electrodes. At 50 mA cm^{-2}, this electrode requires an overpotential of 236 mV, lower than those of the other sulfur-containing samples and the RuO_2/FF reference (Figure.8b). Its Tafel slope of 86 mV dec^{-1} is also the lowest among the samples prepared with both low and high sulfur precursor concentrations (Figs. 8c and 8d), indicating more favorable apparent OER kinetics under the measurement conditions.

The Nyquist plots in Figure.8e show that bare iron foam has the largest overall impedance, whereas S-NiFe(OH)x-0.01/FF exhibits lower impedance than samples prepared with other sulfur precursor concentrations. Together with the structural and spectroscopic results, this observation suggests that the mixed-anion environment contributes to the improved OER performance. Sulfur incorporation may modify the electronic environment of the metal sites and alter the balance between reactant adsorption and product desorption. S-NiFe(OH)x-0.01/FF also shows stable operation during 12 h of galvanostatic testing at 50 mA cm^{-2}, with an overpotential increase of less than 10 mV (Figure.8f). This result demonstrates operational stability over the tested period, although post-test characterization is needed to assess structural and compositional changes.

Figure.8g illustrates the schematic mechanism for enhanced electrocatalytic activity via precise anion modulation. OER is a typical surface reaction consisting of three core steps: reactant adsorption, electron transfer, and product desorption. Accelerating the reaction kinetics of these three steps collectively contributes to improved OER electrocatalytic performance. On one hand, oxygen anions feature strong ionic character, weak electronic interaction and low polarizability, which enable metal cations to generate a strong positive electric field. Such characteristic favors the adsorption of hydroxyl intermediates yet impedes the desorption of gaseous oxygen. On the contrary, sulfur anions with high polarizability induce electron filling of cationic orbitals, which facilitates O_2 desorption but weakens the

adsorption of OH^-. Consequently, precise anion engineering achieves the optimized electronic configuration of active sites and maximizes the OER electrocatalytic activity.

4. Conclusions

A room-temperature immersion corrosion strategy is developed to fabricate sulfur-containing nickel–iron hydroxide electrodes on iron foam with thioacetamide as the sulfur source. Varying the precursor concentration controlled sulfur incorporation and the transition toward crystalline sulfide formation. At low precursor concentrations, the nanosheet morphology was preserved and sulfur was distributed relatively uniformly. Structural and XPS characterization supported changes in the local metal–anion environment. The optimized S-NiFe(OH)x-0.01/FF electrode delivered 50 mA cm^{-2} at an overpotential of 236 mV, outperforming the RuO_2 reference under the tested conditions, and exhibited a Tafel slope of 86 mV dec^{-1}. Its overpotential increased by less than 10 mV during 12 h of operation at 50 mA cm^{-2}. These results demonstrate a simple, mild route for tuning the composition and OER performance of nickel–iron-based electrodes.

Declarations

Author Contribution

P P Gao T Lei and ML Gao wrote the main manuscript text. Q Kong was responsible for most of the experiments and data analysis, while S T Ouyang is resources and partial investigation. QH Chen was conceptualization and validation. All authors reviewed the manuscript.

Acknowledgement

The work knowledge supports from the science and technology innovation Program of Hunan Province Project (2025RC3301) and Regional Joint Fund of Natural Science Research of Hunan Province (2026JJ80710 and 2026JJ80124) and Research Project of the Department of Education of Hunan Province (25B0448).

References

1. Li X, Pan L, Zhang J (2023) Development status evaluation and path analysis of regional clean energy power generation in China. Energy Strategy Reviews 49:101139
2. Arsad SR, Ker PJ, Hannan MA, Tang SGH, R S N, Chau CF, Mahlia TM (2024) I., Patent landscape review of hydrogen production methods: Assessing technological updates and innovations. Int J Hydrog Energy 50:447–472
3. Mei J, Deng Y, Cheng X, Wang X, Wu Q (2024) Recent advances in iron-based sulfides electrocatalysts for oxygen and hydrogen evolution reaction. Chin Chem Lett 35(1):108900

4. Bhosale M, Baby N, Magdum SS, Murugan N, Kim YA, Thangarasu S, Oh T-H (2024) Hierarchical nanoassembly of Ni3S2-MoS2 interconnected with CeO2 as a highly remarkable hybrid electrocatalyst for enhancing water oxidation and energy storage. J Energy Storage 80:110301
5. Li Y, Mao Z, Wang Q, Li D, Wang R, He B, Gong Y, Wang H (2020) Hollow nanosheet array of phosphorus-anion-decorated cobalt disulfide as an efficient electrocatalyst for overall water splitting. Chem Eng J 390:124556
6. Wang X, Vasileff A, Jiao Y, Zheng Y, Qiao S-Z (2019) Electronic and Structural Engineering of Carbon-Based Metal-Free Electrocatalysts for Water Splitting. Adv Mater 31(13):1803625
7. Sun H, Lian Y, Yang C, Xiong L, Qi P, Mu Q, Zhao X, Guo J, Deng Z, Peng Y (2018) A hierarchical nickel–carbon structure templated by metal–organic frameworks for efficient overall water splitting. Energy Environ Sci 11(9):2363–2371
8. Zhao Z, Yuan Z, Fang Z, Jian J, Li J, Yang M, Mo C, Zhang Y, Hu X, Li P, Wang S, Hong W, Zheng Z, Ouyang G, Chen X, Yu D (2020) In Situ Activating Strategy to Significantly Boost Oxygen Electrocatalysis of Commercial Carbon Cloth for Flexible and Rechargeable Zn-Air Batteries. Adv Sci 7(11):2001501
9. Zhao J, Rong F, Yao Y, Fan W, Li M, Yang Q (2018) Co NP/NC hollow nanoparticles derived from yolk-shell structured ZIFs@polydopamine as bifunctional electrocatalysts for water oxidation and oxygen reduction reactions. J Energy Chem 27(4):1261–1267
10. Tang C, Wang B, Wang H-F, Zhang Q (2017) Defect Engineering toward Atomic Co–Nx–C in Hierarchical Graphene for Rechargeable Flexible Solid Zn-Air Batteries. Adv Mater 29(37):1703185
11. Guo Y, Yuan P, Zhang J, Hu Y, Amiinu IS, Wang X, Zhou J, Xia H, Song Z, Xu Q, Mu S (2018) Carbon Nanosheets Containing Discrete Co–Nx–By–C Active Sites for Efficient Oxygen Electrocatalysis and Rechargeable Zn–Air Batteries. ACS Nano 12(2):1894–1901
12. Luo X, Zhao H, Tan X, Lin S, Yu K, Mu X, Tao Z, Ji P, Mu S (2024) Fe-S dually modulated adsorbate evolution and lattice oxygen compatible mechanism for water oxidation. Nat Commun 15(1):8293
13. Gao GJ, Xu JL, Zhang LW, Ma YC, Luo JM (2023) One-step gas phase sulfided NiFe coating as self-supporting electrode for high efficiency oxygen evolution reaction. Int J Hydrog Energy 48(58):22101–22112
14. Zhao C-X, Li B-Q, Zhao M, Liu J-N, Zhao L-D, Chen X, Zhang Q (2020) Precise anionic regulation of NiFe hydroxysulfide assisted by electrochemical reactions for efficient electrocatalysis. Energy Environ Sci 13(6):1711–1716
15. Wang H-F, Tang C, Li B-Q, Zhang Q (2018) A review of anion-regulated multi-anion transition metal compounds for oxygen evolution electrocatalysis. Inorg Chem Front 5(3):521–534
16. Wu Z, Zhao Y, Wu H, Gao Y, Chen Z, Jin W, Wang J, Ma T, Wang L (2021) Corrosion Engineering on Iron Foam toward Efficiently Electrocatalytic Overall Water Splitting Powered by Sustainable Energy. Adv Funct Mater 31(17):2010437
17. Kong Q, Li Y, Fan N, Guan H, Dong C, Chen G (2020) In situ growth novel cubic copper hydroxyl phosphate and its utilization as a highly sensitive hydrogen peroxide amperometric sensor. Mater

Today Commun 24:101212

18. Wang H, Zeng Z, Xu P, Li L, Zeng G, Xiao R, Tang Z, Huang D, Tang L, Lai C, Jiang D, Liu Y, Yi H, Qin L, Ye S, Ren X, Tang W (2019) Recent progress in covalent organic framework thin films: fabrications, applications and perspectives. Chem Soc Rev 48(2):488–516
19. You B, Sun Y (2016) Hierarchically Porous Nickel Sulfide Multifunctional Superstructures. Adv Energy Mater 6(7):1502333

Figures

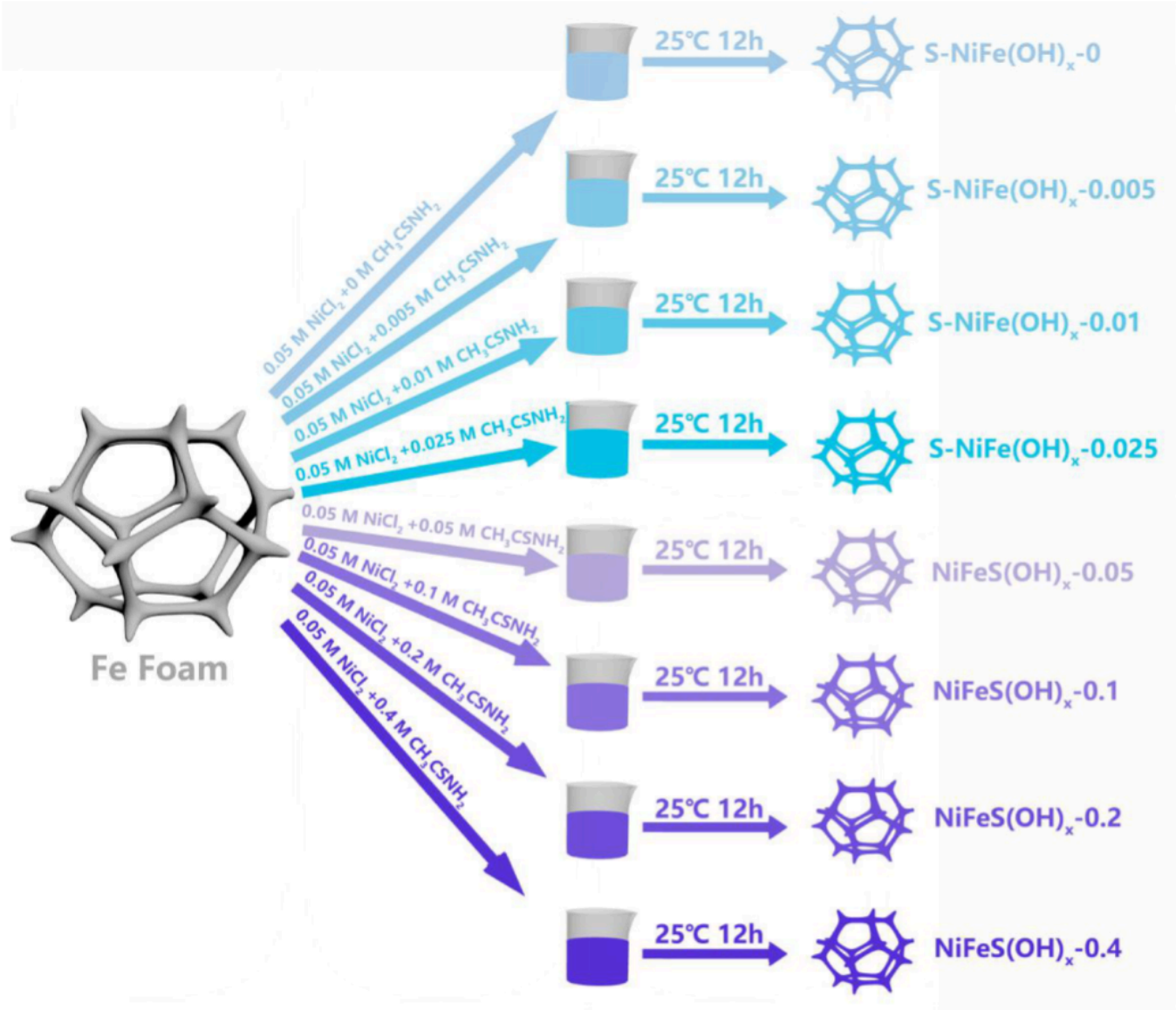

Figure 1

The schematic illustration of the preparation process for the S-NiFe(OH)x/FF and NiFeS(OH)x/FF.

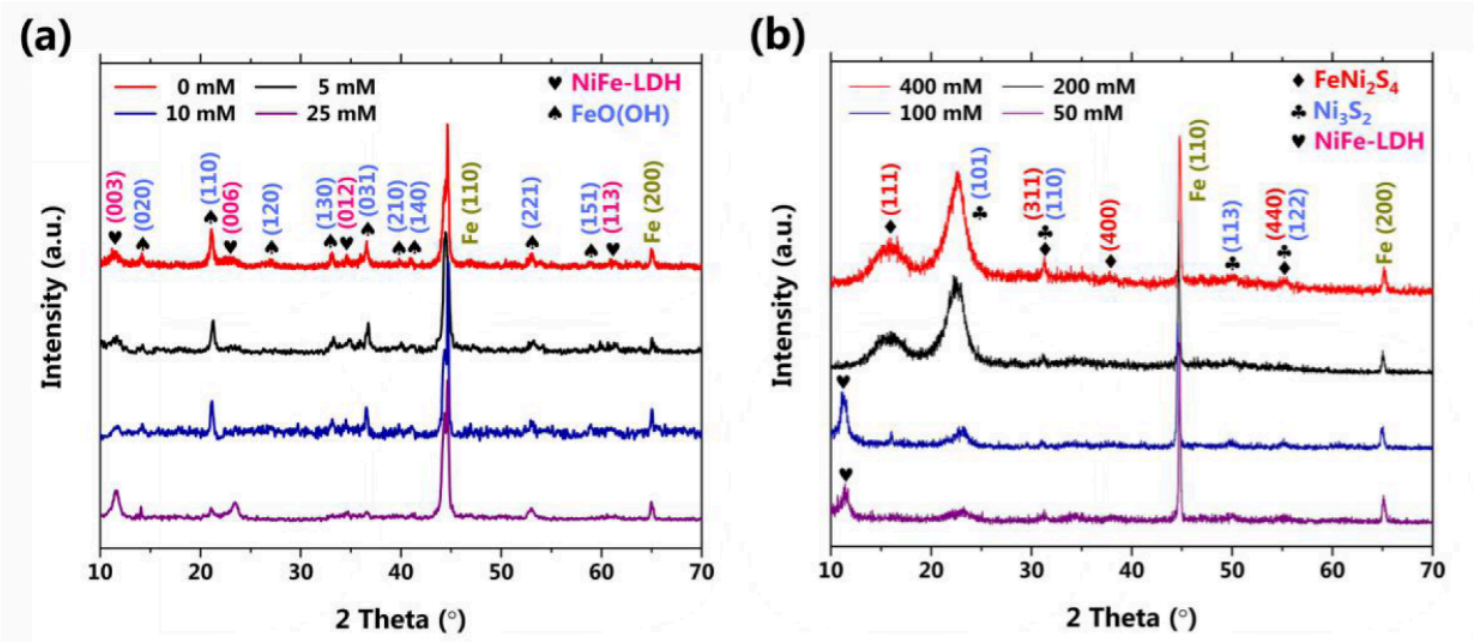

Figure 2

(a-b) XRD patterns of S-NiFe(OH)x/FF samples prepared with different sulfur source concentrations.

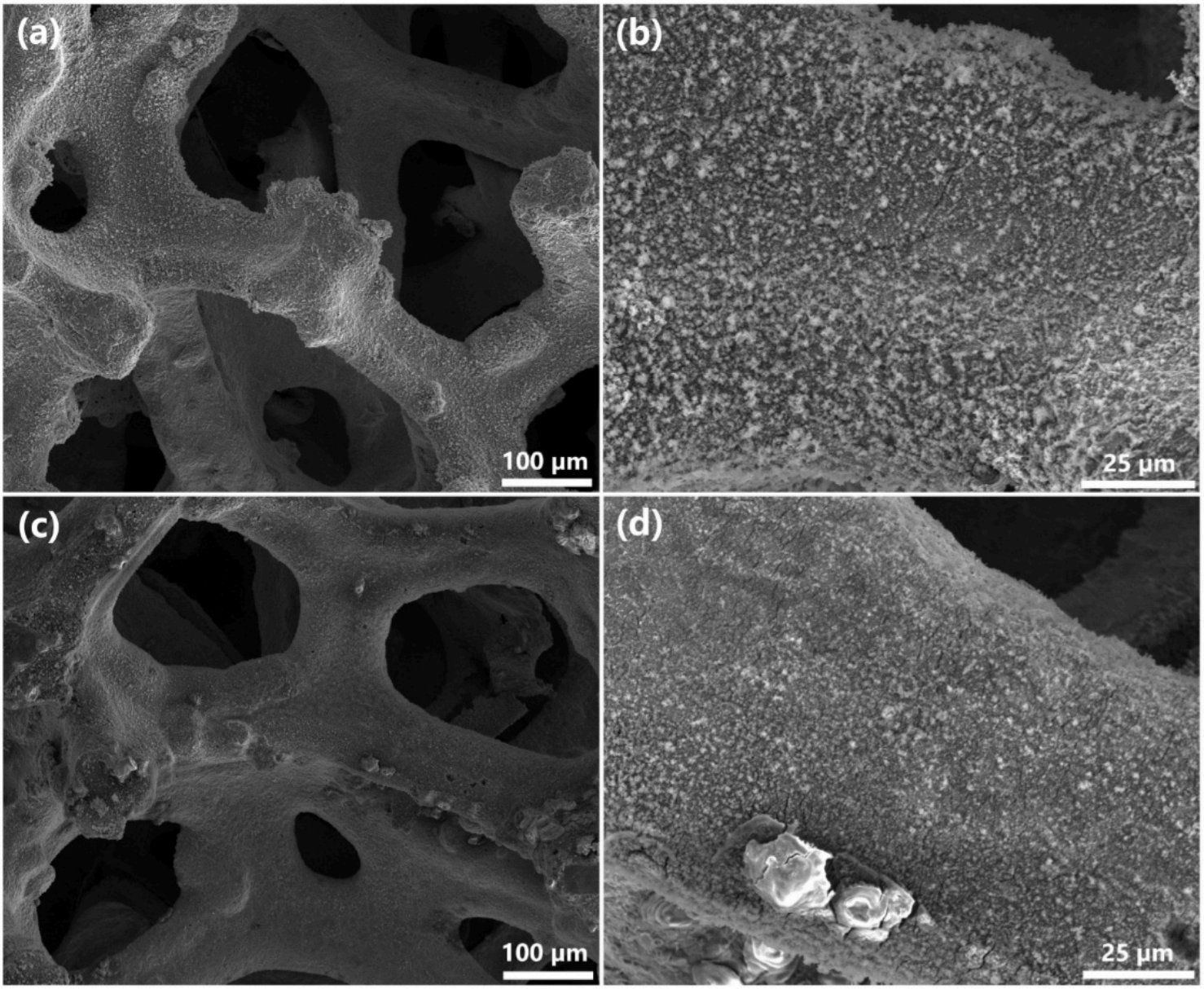

Figure 3

SEM images of S-NiFe(OH)x-0.01/FF samples (a~b) and NiFeS(OH)x-0.4(c~d) with low and hig-resolution.

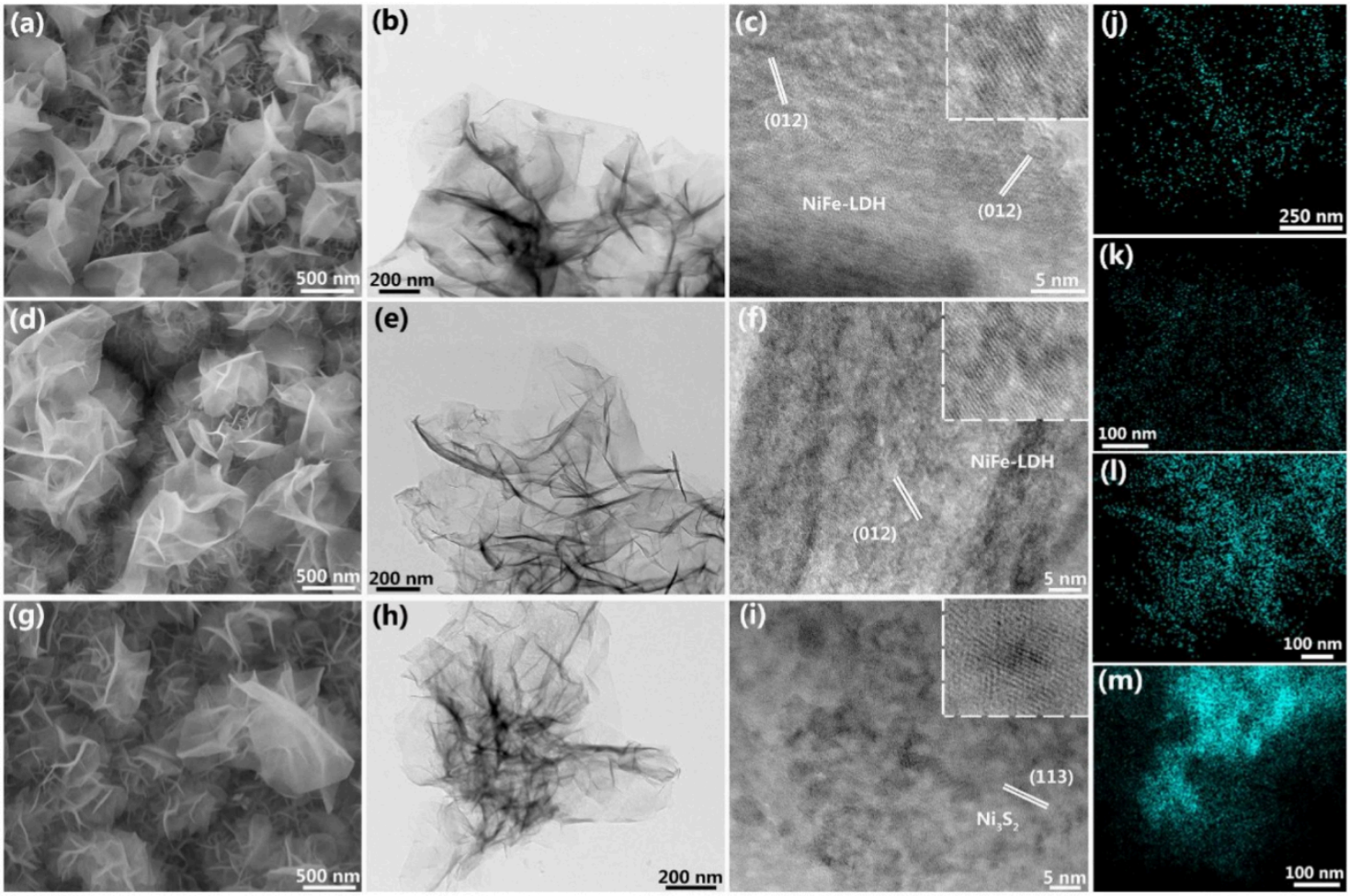

Figure 4

SEM and TEM images of S-NiFe(OH)x/FF samples with low concentrations sulfur source concentrations. (a-c) S-NiFe(OH)x-0; (d-f) S-NiFe(OH)x-0.01; (g-i) S-NiFe(OH)x-0.025. TEM Mapping of S element in (j) S-NiFe(OH)x -0.005, (k) S-NiFe(OH)x -0.01, (l) S-NiFe(OH)x-0.025 and (m) NiFeS(OH)x-0.05.

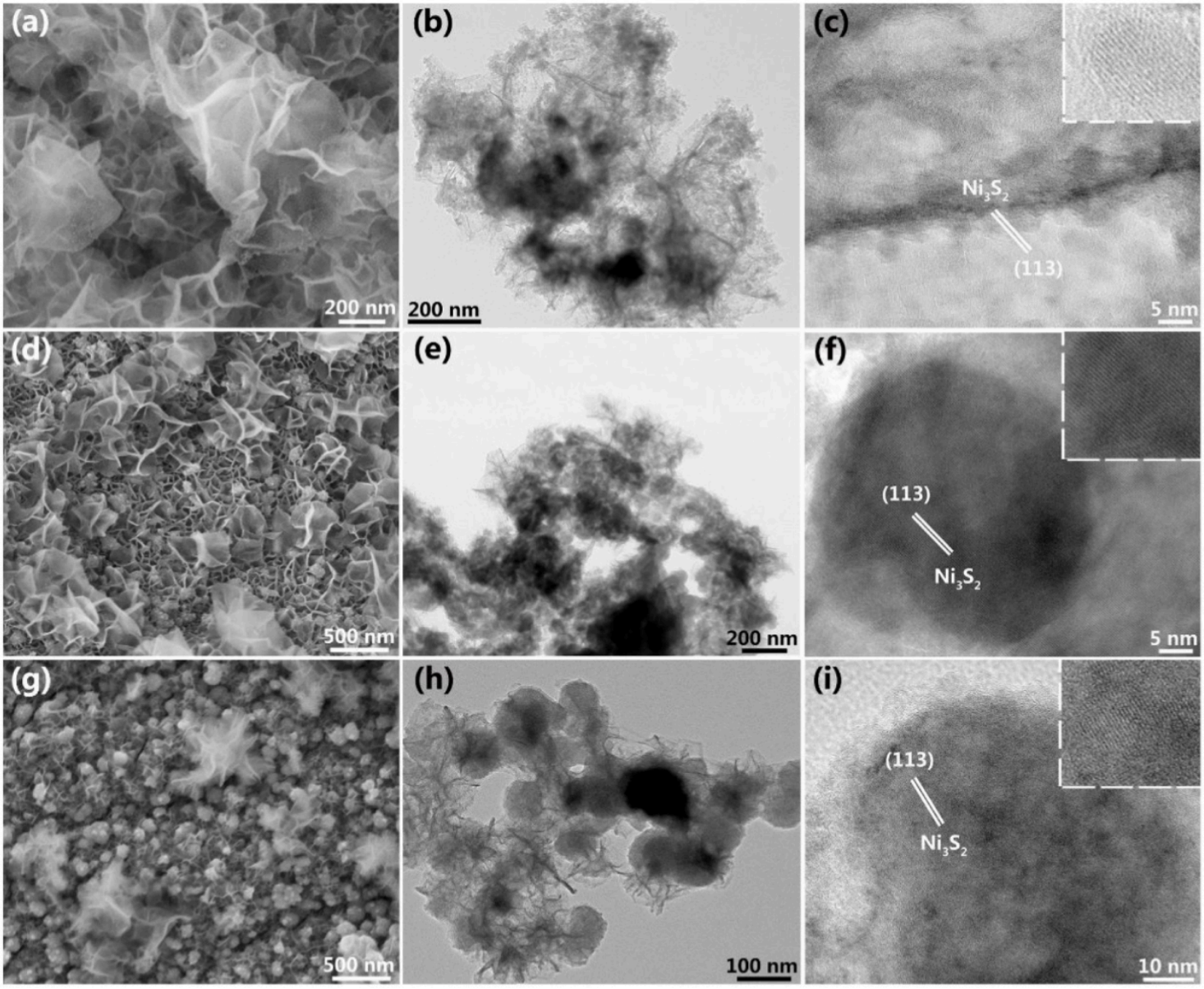

Figure 5

SEM and TEM images of S-NiFeLDH/FF samples with high concentrations sulfur source concentrations. (a-c) NiFeS(OH)x-0.1, (d-f) $NiFeS(OH)_x$-0.2, (g-i) $NiFeS(OH)_x$-0.4.

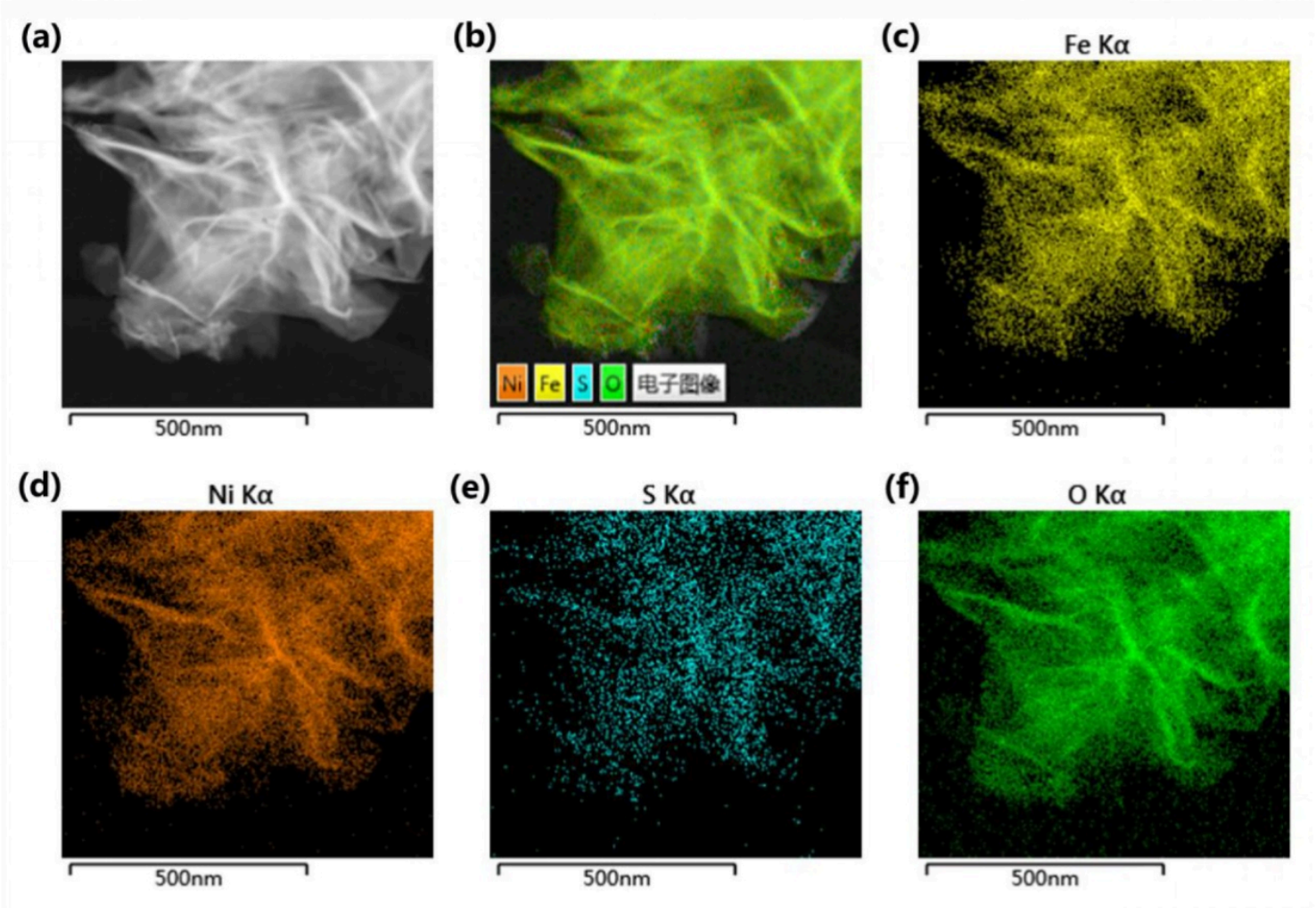

Figure 6

TEM EDS Mapping images of S-NiFe(OH)$_x$-0.01 samples. (a) TEM image, (b) EDS layered image, (c) Fe Kα, (d) Ni Kα, (e)S Kα, (f) O Kα

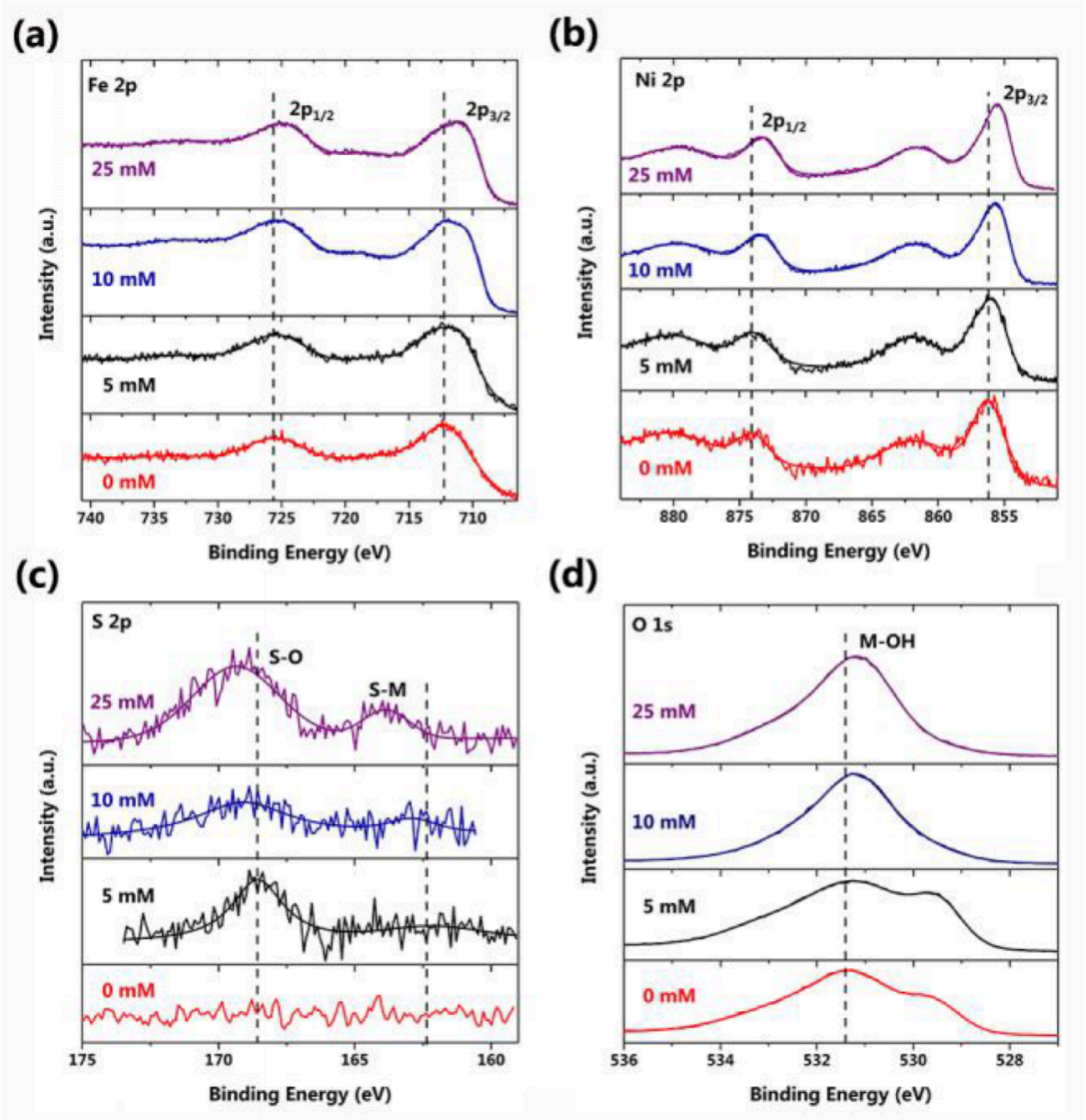

Figure 7

XPS characterization of(a)S 2p, (b)O 1s, (c)Fe 2p and (d) Ni 2p, spectra of S- NiFe(OH)x -0, S- NiFe(OH)x -0.005, S-NiFe(OH)x -0.01 and S- NiFe(OH)x-0.025 samples.

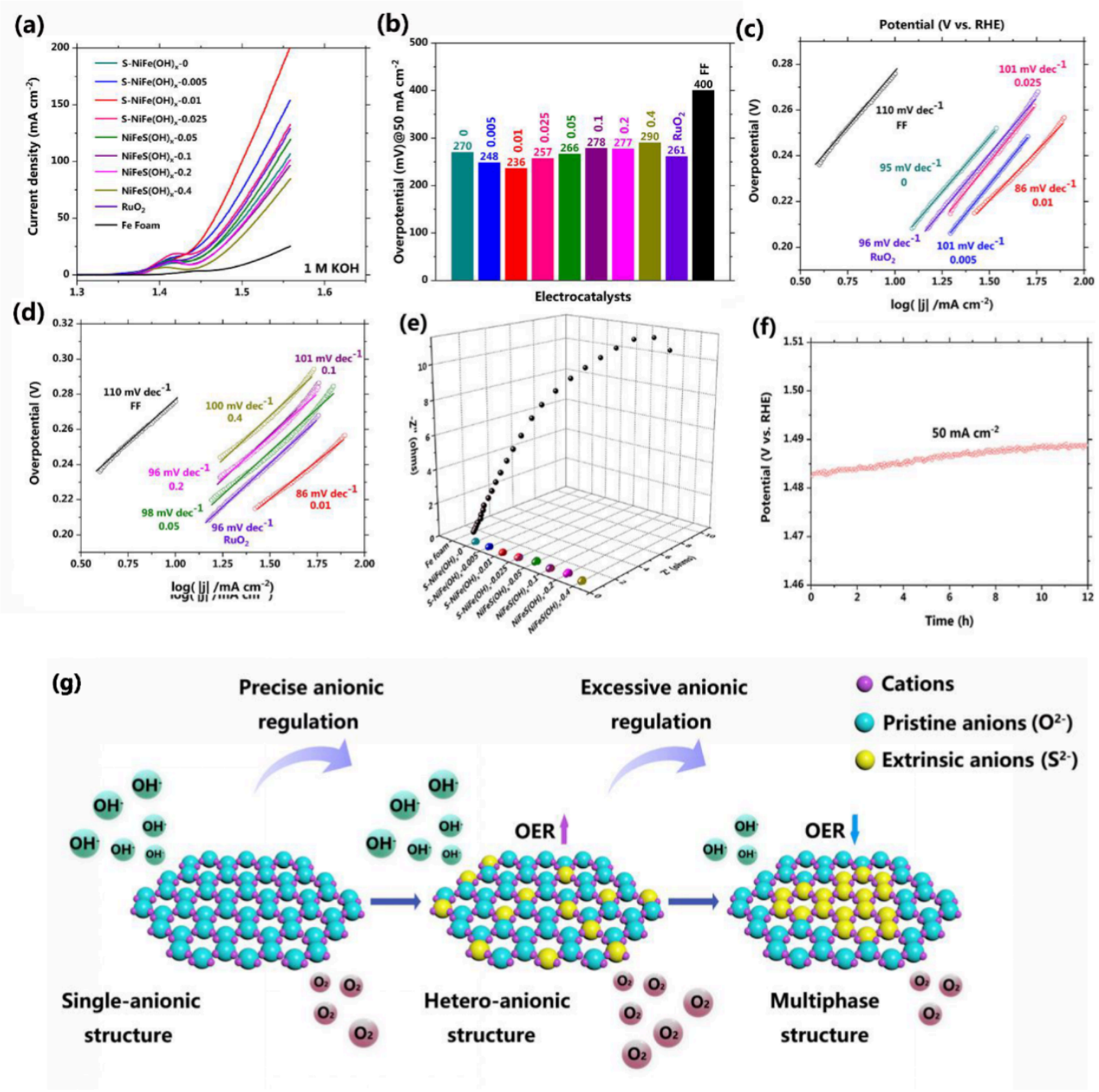

Figure 8

OER electrocatalysis in 1 M KOH. (a) The LSV curves, (b)η_{-50} and (c-d) Tafel plots of S-NiFe(OH)$_x$/FF (or NiFeS(OH)x/FF) along with bare NF and RuO_2 on NF for comparison. (e) EIS spectra of the tested electrodes; and (f) chronopotentiometric stability test of S-NiFe(OH)x/FF at 50 mA cm^{-2}. (g) Proposed mechanism of enhanced OER activity through anion modulation.